Normal mode description of phases of matter: Application to heat capacity

Jaeyun Moon, Simon Thébaud, Lucas Lindsay, Takeshi Egami

Normal mode description of phases of matter: Application to heat capacity

Jaeyun Moon,[1,2,*] Simon Thébaud,[1,3] Lucas Lindsay,[1] and Takeshi Egami[1,4,5]

[1]*Materials Science and Technology Division, Oak Ridge National Laboratory, Oak Ridge, Tennessee 37831, USA*
[2]*Sibley School of Mechanical and Aerospace Engineering, Cornell University, Ithaca, New York, 14853, USA*
[3]*INSA Rennes, Institut Foton, UMR 6082, 35700 Rennes, France*
[4]*Department of Materials Science and Engineering, University of Tennessee, Knoxville, Tennessee 37996, USA*
[5]*Department of Physics and Astronomy, University of Tennessee, Knoxville, Tennessee 37996, USA*

(Received 11 July 2023; accepted 25 January 2024; published 26 February 2024)

Understanding thermodynamics in liquids at the atomic level is challenging because of strong atomic interactions and lack of spatial symmetry. Recent prior theoretical works have focused on describing heat capacity of liquids in terms of phonon-like excitations but often rely on fitting factors and *ad hoc* assumptions. In this work, we propose characterizing various phases in terms of instantaneous normal modes (INMs) of structural snapshots from molecular dynamics simulations of single-element systems over wide ranges of temperature and pressure. We use the INMs to build a mode-level microscopic description of heat capacity and demonstrate that heat capacity of liquids can be described by a combination of both solidlike and gaslike degrees of freedom, leading to a more unified framework to fundamentally describe heat capacity of all three phases of matter: solid, liquid, and gas.

DOI: 10.1103/PhysRevResearch.6.013206

I. INTRODUCTION

In various applications of liquids from nuclear reactors [1] to thermal energy storage systems [2], device performance and efficiency are directly controlled by thermal properties such as heat capacity. However, engineering and customization of thermal properties of liquids are challenging due to a general lack of microscopic understanding of the atomic dynamics in liquids. Liquids have dynamically disordered structures that lack spatial periodicity, yet their physical densities are similar to solids. Gases are similarly disordered but atoms are nearly free. In contrast, atoms in liquids are strongly interacting and dynamically correlated. These complexities strongly challenge accurate characterization of the atomic degrees of freedom in liquids and the development of microscopic theories for liquids.

Unlike liquids, solids (periodic crystals in particular) have a rigorous, microscopic theoretical foundation to describe atomic motion and various materials properties based on normal mode lattice dynamics [3–5]. These properties can now be predicted with high accuracy from routine lattice dynamics calculations [6,7]. In normal mode analysis, one obtains normal mode frequencies and eigenvectors from diagonalization of dynamcal matrices built from second derivatives of the interatomic potential (i.e., harmonic force constants) of a given structure. Normal mode frequencies depict local potential curvatures: modes with imaginary frequencies and real frequencies correspond to negative and positive curvatures of the potential, respectively, while eigenvectors describe constituent harmonic motions. Therefore, normal modes can indicate thermodynamic stability of a given solid phase: imaginary modes imply a structure is dynamically unstable, i.e., another underlying arrangement of atoms is favored for a given interatomic potential [8].

Recently, there has been much interest in extending the normal mode analysis to liquid systems where instantaneous structures are used instead of the equilibrium lattice [9–17]. Normal mode decomposition of atomic motion has the potential to be useful as the number of normal modes in the system is equal to the number of atomic degrees of freedom, $3N = N_{\text{total}} = N_i + N_r$, where N is the number of atoms, N_{total} is the total number of normal modes, N_i is the number of imaginary modes, and N_r is the number of real modes. Therefore, characterization of normal modes can provide insights into the nature of atomic degrees of freedom in materials of interest. From instantaneous structures, a large number of imaginary modes are observed in the normal mode spectra of liquids and various aspects of these imaginary modes have been used to describe nonequilibrium processes including atomic diffusion [12,18] and melting [19] with varying degrees of success. Notably, prior works have attempted to relate self-diffusion coefficients, D, of liquids to the fraction of imaginary modes over the total number of modes [12,20,21]. Some have argued that D is directly proportional to this fraction [12], while others have argued for more subtle relations between D and the fraction of "delocalized" imaginary modes [21]. However, the relationship between imaginary modes and diffusion remains unclear [14], and these works suffer from narrow temperature ranges that have been studied. These examples of using normal modes in describing phase stability in solids and nonequilibrium processes in liquids indicate that characteristics and distributions of normal modes could potentially be

*Corresponding author: jaeyun.moon@cornell.edu

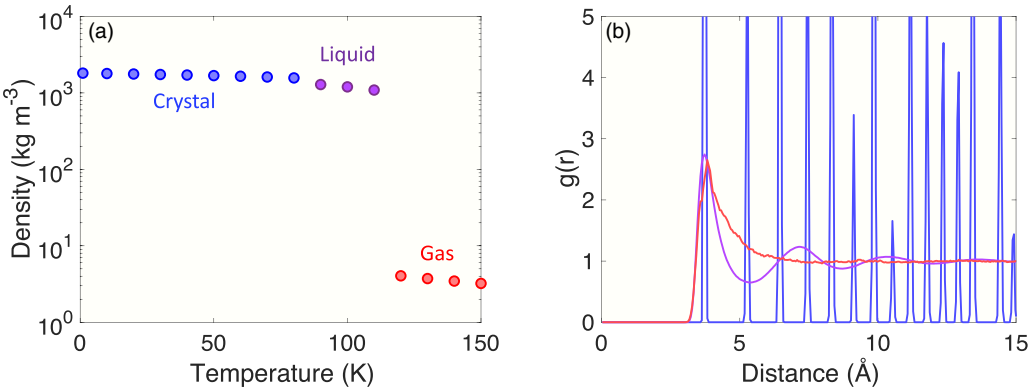

FIG. 1. (a) Temperature-dependent density of LJ argon from 1 K to 150 K at 1 bar, which covers all three phases: crystal (blue circles), liquid (purple circles), and gas (red circles). Error bars which denote standard deviations from ensemble averages are smaller than the symbols. (b) Representative pair distribution function, $g(r)$, of crystal (1 K), liquid (90 K), and gas (120 K) LJ argon.

used as a general descriptor of structural stability and phases beyond limited cases within solids and liquids.

In this work, we extend normal mode analysis to gas phases of single-element systems and find that equal number of real and imaginary modes implies a gas phase using molecular dynamics simulations and lattice dynamics calculations. We propose that atomic dynamics in liquids can be interpreted as an interpolation between solidlike ($N_i = 0$) and gaslike ($N_i = N_{\text{total}}/2$) motions as evident from their respective normal mode spectra. From these, we define instability factors, IF and IF_{alt}, to characterize the material phase, solid (IF ~ 0), liquid ($0 \lesssim \text{IF} < 1$), and gas (IF $= 1$). We further use these instability factor descriptors to build a model for the constant volume-specific heat ranging from solid through liquid to gas phases and test this interpretation against independently calculated specific heat values for a number of systems. Our work, therefore, paves the way towards describing all classical phases of matter under a unified, microscopic framework.

This paper is organized as follows: In Sec. II A we first look at normal mode distributions of argon at 1 bar from solid to gas and introduce instability factors to characterize phases of matter. In Sec. II B we perform lattice dynamics calculations on various single-element systems (argon, iron, and silicon) with constant volumes and obtain their respective instability factors. In Sec. II C a heat capacity model using instability factors is developed and compared against independently calculated constant volume specific heats of the single-element systems. In Sec. III we make a connection between instantaneous normal mode spectra and velocity autocorrelation function spectra through instability factors and discuss implications of our work in the context of prior instantaneous normal mode works. Finally, a summary is given in Sec. IV.

II. SIMULATION DETAILS AND RESULTS

A. Normal modes of argon at 1 bar from solid to gas

We first perform molecular dynamics (MD) simulations of argon (1372 atoms) using a Lennard-Jones potential [22–24] and large-scale atomic/molecular massively parallel simulator (LAMMPS) [25] to generate equilibrated atomic structures from 1 to 150 K under NPT (constant number of atoms, pressure, and temperature) ensemble at 1 bar. Total system volume is allowed to change. Periodic boundary conditions are applied. For each temperature, structures were equilibrated for 1 ns to ensure thermal equilibrium before data collection of another 1 ns with a time step of 1 ps. Ten snapshots distributed evenly within this 1 ns were then used for lattice dynamics calculations (GULP [7]), and normal mode spectra were averaged over these 10 snapshots. Resulting temperature-dependent densities are shown in Fig. 1(a). We observe discontinuities between 80 and 90 K and 110 and 120 K, marking the phase transitions from crystal to liquid and liquid to gas phases, consistent with prior studies. Representative pair distribution functions, $g(r) = \frac{1}{4\pi N n r^2} \sum_{i,j} \langle \delta(r - |\boldsymbol{r}_i - \boldsymbol{r}_j|) \rangle$, for crystal (1 K), liquid (90 K), and gas (120 K) argon are shown in Fig. 1(b). Here N is the number of atoms, n is the number density, $\boldsymbol{r}_i$ is the atomic position of the ith atom, and the angled bracket denotes an ensemble average. As expected for crystals, we see sharp face-centered cubic peaks. Broadened peaks and valleys are observed for the liquid phase, and the pair distribution function eventually damps out to unity with increasing distance. These peaks and valleys disappear for the gas systems, indicating loss of structural correlation except for weak pile-up at the contact distance.

From the snapshot structures of various phases, we perform lattice dynamics calculations to obtain normal mode frequencies (ω_n) and eigenvectors ($\boldsymbol{e}_n$) from Γ-point dynamical matrices ($\boldsymbol{D}$) as

$$\omega_n^2 \cdot \boldsymbol{e}_n = \boldsymbol{D} \cdot \boldsymbol{e}_n, \tag{1}$$

where subscript n denotes a mode number from 1 to $3N$ ($N = 1372$) and dynamical matrices are related to the potential (U) by

$$D_{\alpha\beta,ij} = \frac{1}{\sqrt{m_i m_j}} \frac{\partial^2 U}{\partial u_{\alpha,i} \partial u_{\beta,j}}, \tag{2}$$

where m_i is the mass of atom i and Greek subscripts denote Cartesian directions. Resulting representative normal mode densities of states, INM(ω), for LJ argon in crystal (1 K), liquid (90 K), and gas (120 K) phases are shown in Fig. 2(a). For crystalline argon, all normal modes are real at low temperatures, and the density of states has sharp kinks, representing van Hove singularities typically observed near the Brillouin

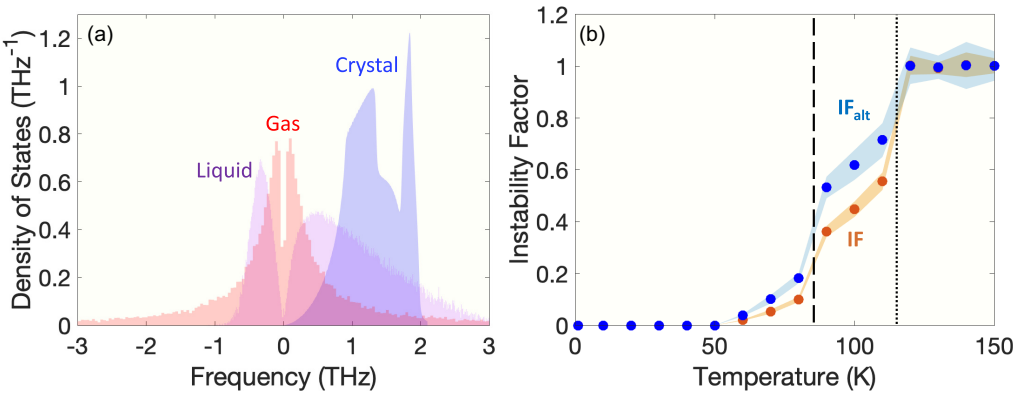

FIG. 2. (a) Representative normal mode densities of states for crystal (1 K), liquid (90 K), and gas (120 K) LJ argon. Normal mode frequencies are multiplied by a factor of 500 for the gas phase for better visualization. (b) Instability factors proposed as a descriptor of phase of matter as a function of temperature. Vertical dashed (crystal to liquid) and dotted lines (liquid to gas) represent phase transitions. Shaded areas represent error limits determined from standard deviations from ensemble averages.

zone boundaries. For liquid argon, a significant number of imaginary modes (they are shown as having negative frequencies) start to appear as commonly observed in liquids. There is weak temperature dependence (not shown here) on the number of imaginary modes observed in the liquid phase; however, real modes dominate the density of states as measured by the area under the curve. For argon gas, a long potential cutoff distance on the order of half the domain size was necessary to build dynamical matrices satisfying translational invariance, which leads to three Goldstone modes at 0 THz similar to solids and liquids. Corresponding normal mode density of states for gas argon at 120 K is shown in Fig. 2(a). Interestingly, we have an equal number of real and imaginary modes for gas phases irrespective of temperature. As normal mode analysis is typically used for solids, real modes in liquids have been considered to derive from harmonic oscillators similar to solids [19,26]. However, interpreting the real frequency modes in high-temperature gases as conventional phonon harmonic oscillators is highly questionable. Recently, our work has explicitly shown that some of these real frequency modes in instantaneous normal mode spectra are collisional and translational in nature, similar to real atom gas dynamics [17].

We note that our calculations demonstrate that imaginary modes are nearly half the modes observed at high temperatures in the gas limit, while relaxed and stable solids have only real modes. The square of the instantaneous normal mode frequency reflects the curvature of the local potential energy landscape (PEL) that atoms participating in the normal mode see at that instant, i.e., the MD snapshot. PEL [27] is usually applied to the whole system, but here we focus only on the portion of PEL involved in the normal mode. Considering subsystems of the PEL is not new. For instance, when a relaxation of a glass is considered, only the atoms that are involved in the relaxation phenomenon are taken into account in depicting the PEL [27,28]. At low temperatures the system is largely trapped in the valleys of the PEL with positive curvatures, so the instantaneous normal mode frequencies are real. In contrast, at very high temperatures the system samples configurational space with positive curvatures (valleys) as well as the positions with negative curvatures (hills) equally. In addition, from random matrix theory, eigenvalue distribution of symmetric sparse random matrices results in Wigner's semicircle law with an even number of positive and negative eigenvalues [29]. As matrix elements for gas systems are more randomized than those of solids and liquids, it is reasonable that the number of positive and negative eigenvalues are equal for dynamical matrices of high temperature gases.

To describe this transition of instantaneous normal mode spectra from solid to gas, we propose two phenomenological instability factors (IF and IF$_{alt}$) built from the microscopic mode characteristics as a measure of how unstable the system is in the configurational space as

$$\mathrm{IF} = \frac{N_i}{N_r}, \tag{3}$$

$$\mathrm{IF}_{\mathrm{alt}} = \frac{2N_i}{N_i + N_r}. \tag{4}$$

IF represents the ratio of the number of imaginary modes to that of real modes, and IF$_{alt}$ is linearly related to the fraction of the PEL with negative curvatures that the system sees. For a relaxed solid (i.e., not near a phase transition), both instability factors are zero, while for a gas both are unity. Liquid instability factors fall between these two limits. Therefore, the instability factors proposed here are a measure of "gasness" in the system. These instability factors describe phases of matter in a continuous, normalized manner and provide an emergent pathway to understand mode-resolved thermodynamic behaviors of liquid states.

Temperature-dependent instability factor values for our LJ argon system at 1 bar are shown in Fig. 2(b). Instability factors increase with temperature and saturate at 1 above the liquid-gas phase transition. We do observe some imaginary modes for solids near melting due to instability of the largely perturbed crystalline structure. Perhaps corresponding instability factors could be used as a crystal-liquid phase transition criterion similar to Lindemann's melting criterion [30–32], where the root mean square of the particle displacements from the equilibrium positions reaches ∼10% of the interatomic distance.

To test our interpretation of normal modes describing phases of matter, we propose a constant volume-specific heat model from solid to gas of various single-element materials

(argon, silicon, and iron) in terms of instability factors, and compare against independently computed specific heat from molecular dynamics energy fluctuations. These systems have different atomic structures in the solid state: face-centered cubic (argon), face-centered cubic (silicon), and body-centered cubic structures (iron) below melting temperatures under atmospheric pressures. Upon melting, liquid argon and iron atoms are closely packed with coordination numbers around 13 to 14. In comparison, silicon possesses more complex temperature-dependent structural features. Due to formation of metallic bonds upon melting, the coordination number of silicon increases from 4 to 6 or more, and there also exists a low-density liquid to high-density liquid transition, commonly observed in other tetrahedral systems including water. Both structural changes in silicon have been well characterized by the Stillinger-Weber potential used here. Having the various structural features and bond natures described above, argon, silicon, and iron are versatile test systems for the purpose of this study.

In real systems, anharmonicity in the interatomic potential plays an important role in how heat carriers interact and how much energy each heat carrier can carry. However, accounting for anharmonicity accurately in a wide range of temperatures is a formidable task even for simple crystals. Rather, for proof of principle here, we focus on idealized systems with constant density ($= \rho_0$, equilibrated at 1 K and 1 bar) from solid to gas where we expect lesser degrees of anharmonicity. Unphysically high temperatures on the order of the temperature of the center of our Sun ($\sim 1.5\times10^7$ K) are, therefore, necessary to reach gas phases.

B. Normal modes of argon, silicon, and iron at constant volume from solid to gas

For argon, FCC structure of 1372 atoms with a lattice parameter of 5.269 Å (ρ_0) was used as an initial input structure for molecular dynamics simulations. Temperatures considered were from 1 to 10^8 K in increments of factors of 10 (log scale) excluding 100 K near the melting temperature. Extremely high temperatures were necessary to reach the gas limit ($C_V = 1.5Nk_B$). MD time steps were 0.1 and 0.01 fs depending on the temperature to capture the fast atomic dynamics. For silicon, FCC structure with 1728 atoms with lattice parameter of 5.431 Å (ρ_0) was employed. Calculations were done at temperatures from 1 to 10^7 K with varying time steps of 0.5 and 0.05 fs. For iron, BCC structure with 2000 atoms with a lattice parameter of 2.867 Å (ρ_0) was studied from 1 to 10^6 K. Time steps of 0.1 and 0.01 fs were used. Interatomic interactions are described by Lennard-Jones (argon) [22–24], Stillinger-Weber (silicon) [33], and modified Johnson potentials (iron) [34,35]. At each temperature, all systems were equilibrated for 5×10^6 time steps in the canonical ensemble (NVT) prior to data recording of another 5×10^6 time steps under the same ensemble. Relativistic corrections were not needed at high temperatures due to relatively heavy masses of our systems. Ten MD snapshot structures are used to compute normal modes. As demonstrated by pair distribution functions above melting temperatures for ρ_0 systems shown in the Appendix Sec. 1, we have various liquid and gas phases.

The same procedures were additionally applied to structures at different densities to characterize the sensitivity of density and anharmonicity: $0.9\rho_0$ and $0.8\rho_0$ for argon, $1.1\rho_0$ for silicon, and $0.9\rho_0$ for iron. Due to a large relative increase in coordination numbers from 4 to 6 and above upon melting for silicon, reducing density to $0.9\rho_0$ and $0.8\rho_0$ led to segregation of atoms and large empty space in the simulation domains for some liquid temperatures. Thus, we instead chose a more dense $\rho = 1.1\rho_0$ for silicon.

Resulting instantaneous normal mode densities of states for all ρ_0 systems beyond the melting temperatures (liquids and gases) are shown in Fig. 3. Lightest blue shades represent lowest temperatures, and the shades become progressively red with increase in temperature. Similar trends are observed for these constant density systems as observed in the LJ argon at 1 bar (see Fig. 2). At the lowest temperatures, INM(ω) for all systems are dominated by real modes as measured by the areas under the curves. As temperature is increased, imaginary mode populations become more prominent, and eventually real and imaginary mode populations become approximately equal. We expect more size effects in INM(ω) compared to our constant pressure argon systems at low frequencies $\omega \lesssim 1$ THz as the model size is fixed. However, low-frequency modes constitute a small portion of the overall mode population and should not generally affect our results. Corresponding instability factors were subsequently calculated for all systems, and temperature-dependent values are described in the Appendix Sec. 2. With these instability factors, we build a heat capacity model next.

C. Specific heat model using instability factors

For canonical ensembles in equilibrium, statistical mechanics dictates that specific heat is related to energy fluctuations by

$$C_V = \frac{\langle E^2\rangle - \langle E\rangle^2}{k_B T^2}, \tag{5}$$

where angled brackets represent ensemble averages. Temperature-dependent specific heats of all systems studied in this work are shown in Fig. 4. Melting temperatures are denoted by the red horizontal lines on the x axis. For molecular dynamics simulations, which are classical, specific heats for solids even at low temperatures are $3Nk_B$ as observed in the figure. We observe clear transitions to the gas limit as we increase the temperature. From these specific heats, comparisons are made against instability factors for various liquid and gas systems as shown in Figs. 5(a) and 5(c). Despite different spectral shapes and features among argon, silicon, and iron systems as demonstrated in Fig. 3, strong correlations between instability factors and heat capacities with small spread are evident irrespective of the system, and specific heats approach $1.5Nk_B$, expected for gas systems around an instability factor equal to unity.

From these correlations between the specific heats and the instability factors, we develop a specific heat model based on the instability factors. We approximate the total energy as the linear combination of those in solidlike (first term) and gaslike

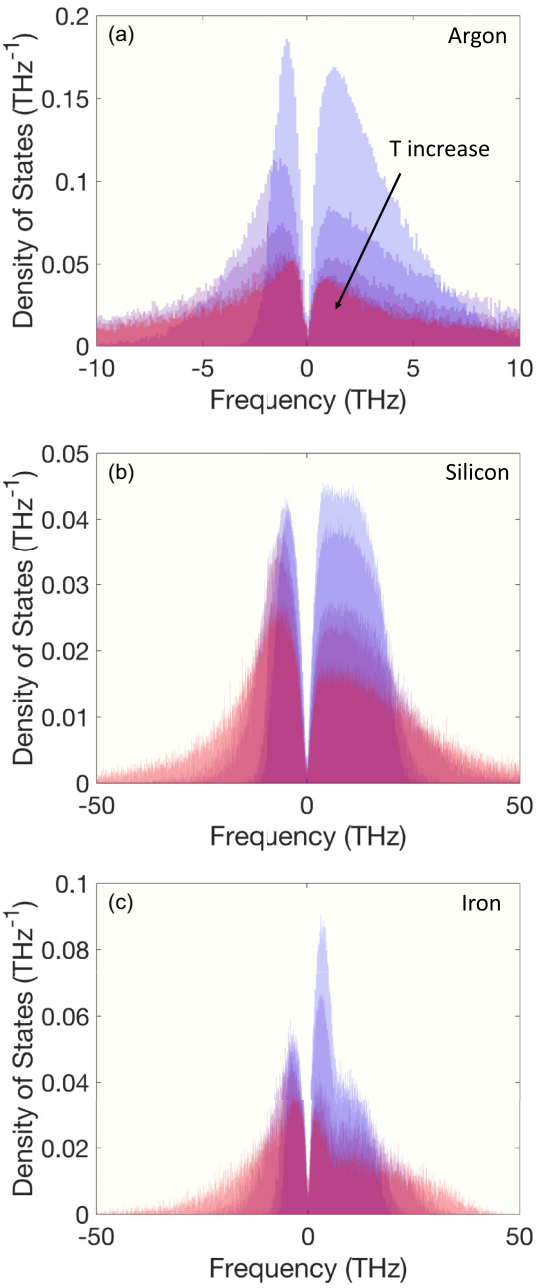

FIG. 3. Instantaneous normal mode density of states [INM(ω)] of (a) argon from 10^3 to 10^8 K, (b) silicon from 5×10^3 to 10^7 K, and (c) iron from 5×10^3 to 10^6 K. All systems were evaluated at ρ_0. Each INM(ω) is normalized such that the integral over the entire frequency range is unity. Lightest blue and darkest red represent lowest and highest temperatures, respectively. Negative frequency means imaginary frequency. At low temperatures, modes with real frequency dominate the spectra. As temperature increases, we observe that imaginary mode populations become more significant.

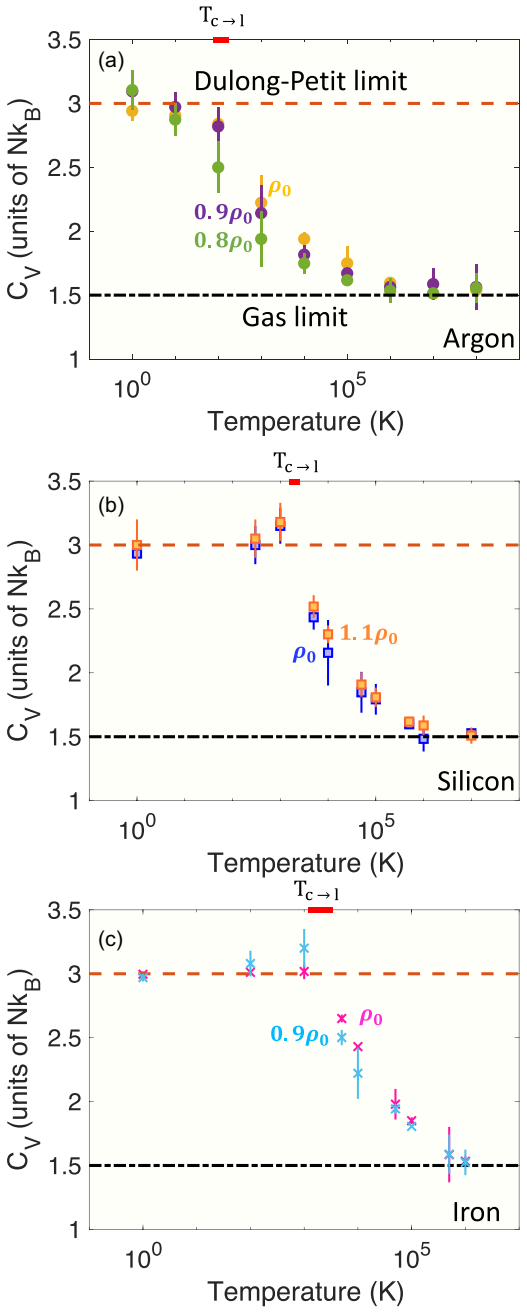

FIG. 4. Temperature-dependent constant volume heat capacity of (a) argon, (b) silicon, and (c) iron with different densities using Eq. (5). Different marker colors represent different densities. Brown dash lines and black dash-dot lines represent Dulong-Petit limits and gas limits for monatomic systems, respectively. $T_{c\to l}$ marked by red lines mean crystal to liquid melting temperatures.

(second term) states,

$$E = (1-x)(3Nk_BT) + x\left(\tfrac{3}{2}Nk_BT\right), \tag{6}$$

where x is either IF [Eq. (3)] or $\mathrm{IF}_{\mathrm{alt}}$ [Eq. (4)]. The corresponding constant volume heat capacity for solids, liquids, and gases under the classical and harmonic approximations is then simply

$$C_V \equiv \left.\frac{dE}{dT}\right|_V = (1-x)(3Nk_B) + x\left(\frac{3}{2}Nk_B\right) - \frac{dx}{dT}\left(\frac{3}{2}Nk_BT\right). \tag{7}$$

The last term in Eq. (7) originates from the fact that instability factors are also temperature dependent.

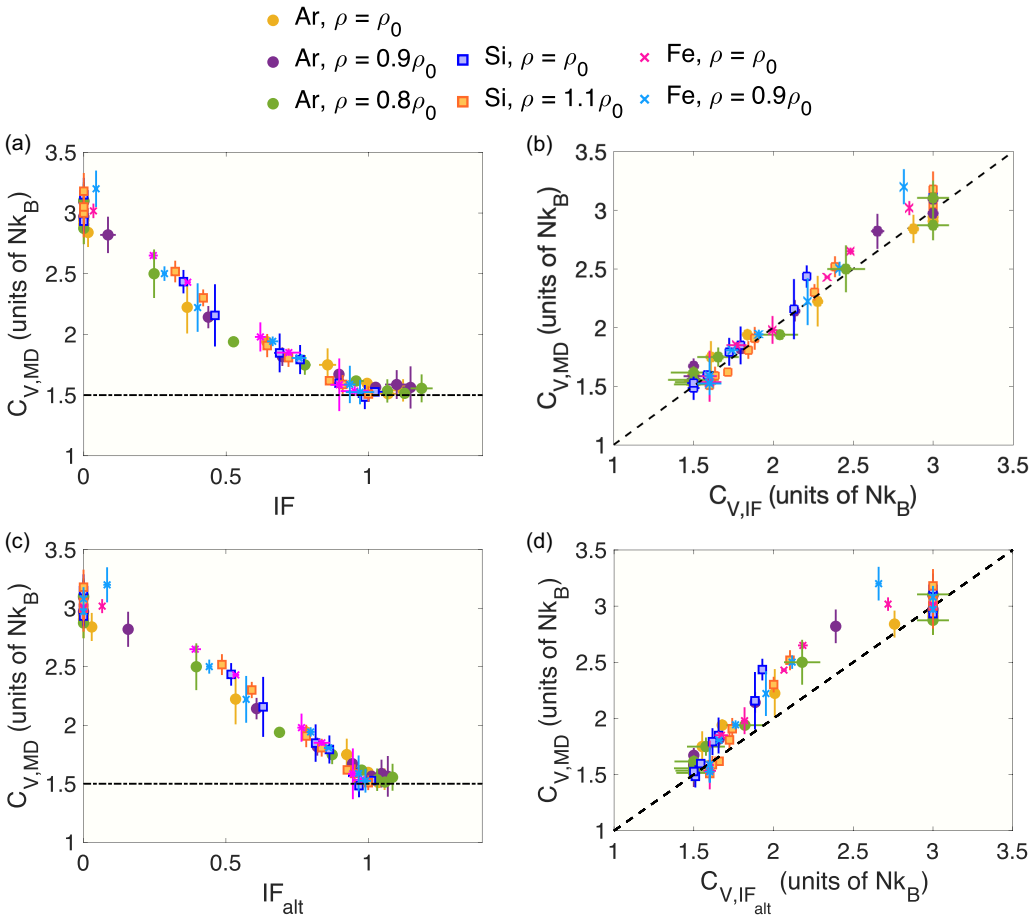

FIG. 5. (a), (c) Heat capacity calculated from molecular dynamics plotted against instability factors, IF and IF_{alt}, for various constant volume materials. Transition to $C_V = 1.5Nk_B$ (dot-dash line) is observed near instability factors at unity. (b), (d) Predicted constant volume heat capacity from instability factors [Eq. (7)], compared to heat capacity from molecular dynamics [Eq. (5)]. Dashed black lines represent one to one correspondence. Good agreement is generally shown within ~5% of error for $C_{V,IF}$.

Instability factor derivatives at each T were found from additional instability factors calculated at adjacent temperatures ($0.9T$ and $1.1T$), i.e., numerical derivatives. Resulting one-to-one comparisons between heat capacities from molecular dynamics [Eq. (5)] and from our proposed model [Eq. (7] for liquids and gases are demonstrated in Figs. 5(b) and 5(d). $C_{V,IF_{alt}}$ tends to underestimate $C_{V,MD}$. In other words, IF_{alt} overestimates the "gasness" in these materials. $C_{V,IF}$ shows a better agreement within 5% of discrepancy against $C_{V,MD}$. In using IF_{alt}, it is intrinsically assumed that imaginary modes are solely responsible for "gasness" in the system and real modes are solidlike. However, in our recent work [17], we have shown that both real and imaginary modes can depict gaslike collisional and translational atomic motion, suggesting that IF may be physically a better choice. Therefore, we focus on IF in subsequent discussions. Agreement between $C_{V,IF}$ and $C_{V,MD}$ within 5% error for various liquid and gas systems gives supporting evidence for our interpretations of normal modes in solid, liquid, and gas phases from a unified perspective via microscopically defined instability factors.

We anticipate two possible sources of error when comparing the specific heat values. The first one is the theory itself, i.e., IF does not represent "gasness" correctly. The other source of error is neglecting anharmonicity in potential interactions that are included in MD simulations. We have shown that at high enough temperatures, thermal atomic motion is large enough that there are imaginary instantaneous modes in solids (see Figs. 2 and 8) and specific heat can also deviate from the Dulong-Petit law, $C_V = 3Nk_B$, as shown in Fig. 4, because thermally vibrating atoms can also sample anharmonic potential energy landscape. The combination of these on heat capacities merits further studies. However, these effects do not appear to have a large influence on the agreement between our model and independently calculated constant volume heat capacity, as shown in Fig. 5. To minimize the effect of volume expansion and contraction on the potential interactions, we have focused our discussion primarily to systems with constant density at ρ_0. We have also computed specific heat and IF for densities slightly different from ρ_0 to examine the sensitivity of volume variations near ρ_0 via instability factors determined by microscopic modal behaviors as shown in Fig. 5. It is apparent that small changes in density do not affect the agreement. We note that our work does not assume Debye or Gaussian densities of states that are often used in the literature [16,36,37]. Rather, we examined the actual INM(ω) from realistic potentials and made connections to specific heats directly. Direct comparison

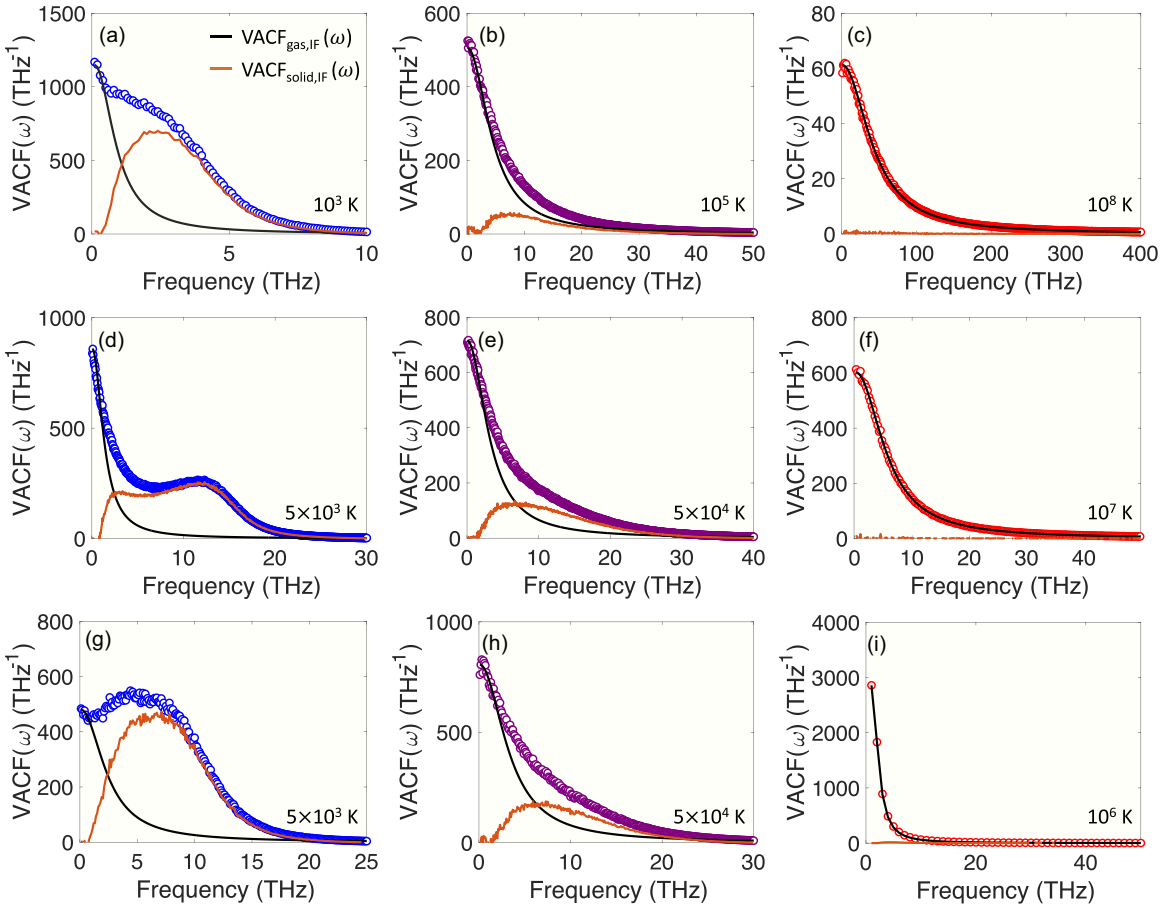

FIG. 6. Decomposition of spectral velocity autocorrelation function, VACF(ω), at select temperatures of (a)–(c) argon from 10^3 to 10^8 K, (d)–(f) silicon from 5×10^3 to 10^7 K, and (g)–(i) iron from 5×10^3 to 10^6 K. All systems were evaluated at ρ_0. Black curves represent spectra of gaslike degrees of freedom, VACF$_{gas}$(ω), from instability factor and orange curves represent spectra of solidlike degrees of freedom, VACF$_{solid}$(ω), obtained from subtraction of VACF(ω) by the black curves.

with experiments is challenging as most heat capacity measurements are done under constant pressure conditions, thus with varying density. Further, it is expected that anharmonicity will be important near melting and glass transition temperatures. Pressure and volume dependence and the role of anharmonicity in heat capacity merit further investigations.

III. DISCUSSION

In addition to INM(ω), velocity autocorrelation function [VACF(ω)] is another useful theoretical tool that yields $3N$ through integrating over frequency. The VACF(ω) describes the phonon density of states for solids under harmonic approximations and is equivalent to INM(ω) [5] as demonstrated in the Appendix Sec. 4 for crystalline silicon at 1 K. VACF(ω) can also describe nonphononic dynamics as VACF($\omega = 0$) represents the self-diffusion coefficient in the system. In our normalization, $D = \frac{k_B T}{12mN}$VACF($\omega = 0$) where D and m represent self-diffusion coefficient and atomic mass, respectively. However, the relationship between INM(ω) and VACF(ω) is not obvious. In INM(ω), curvatures of the potential energy landscape are described through normal modes based on snapshot structures, and we propose to characterize phases of matter in terms of the averaged distribution of normal modes, i.e., IF. On the other hand, VACF(ω) captures time-dependent atomic dynamics more directly. In this work, we attempt to make a connection between INM(ω) and VACF(ω) through our instability factors. In the case of a gas (IF = 1 for our analysis), VACF(ω) is Lorentzian with a peak given by D and integral describing all $3N$ atomic degrees of freedom, with no phonon quasiparticles. For a relaxed solid (IF = 0), VACF(ω) strictly describes phonon density of states, with no free diffusing atoms. Motivated by this contrast, we partition VACF(ω) into a gaslike portion, VACF$_{gas}$(ω), with negligible attractive potential interactions and a solidlike portion, VACF$_{solid}$(ω), with strong potential interactions. We assume that VACF$_{gas}$(ω) has a Lorentzian line shape with the height determined by the diffusion coefficient. Furthermore, its width is chosen such that

$$\frac{1}{3N}\int \text{VACF}_{gas}(\omega)\, d\omega = \text{IF}. \tag{8}$$

VACF$_{solid}$(ω) is then determined by subtracting VACF(ω) by VACF$_{gas}$(ω),

$$\frac{1}{3N}\int \text{VACF}_{solid}(\omega)\, d\omega = 1 - \text{IF}. \tag{9}$$

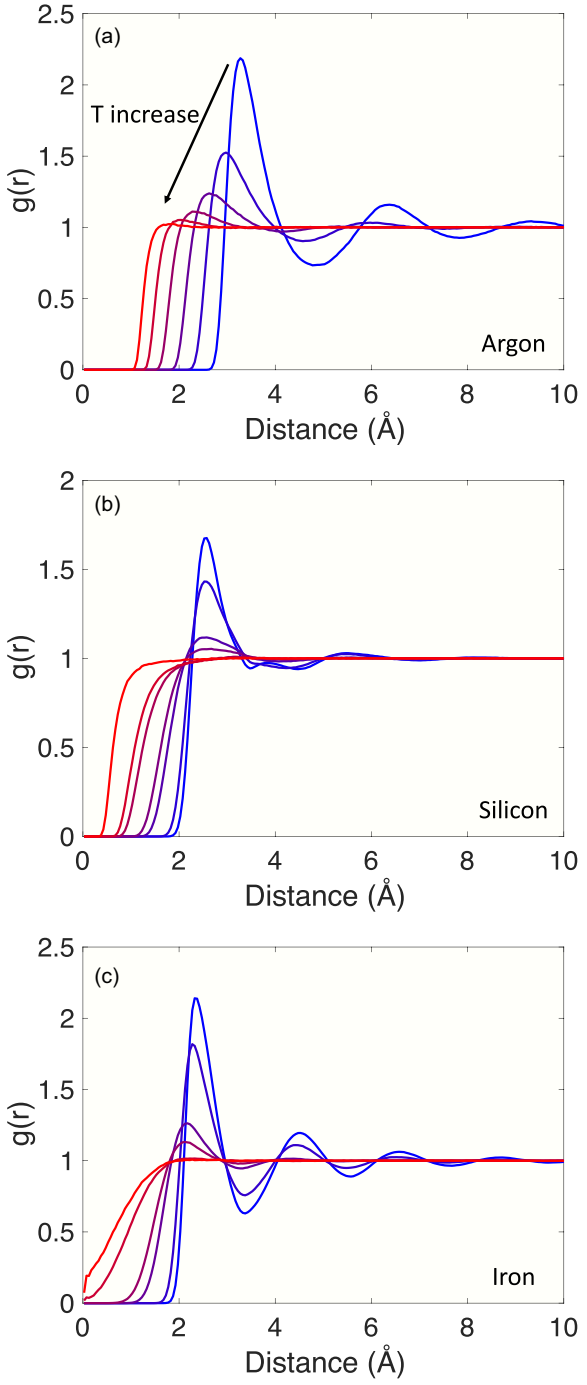

FIG. 7. Pair distribution function, $g(r)$, of (a) argon from 10^3 to 10^8 K, (b) silicon from 5×10^3 to 10^7 K, and (c) iron from 5×10^3 to 10^6 K. All systems were evaluated at ρ_0. Lightest blue and darkest red curves represent lowest and highest temperatures, respectively. Well-defined peaks and valleys in $g(r)$ progressively disappear as temperature increases highlighting transition from liquid states at lower T to gas states at higher temperatures.

The calculated VACF(ω) and corresponding gaslike and solidlike decompositions for all systems at select low, intermediate, and high temperatures are shown in Fig. 6. If the "gasness" in the system is severely overpredicted, hence affecting the Lorenzian line width, $\text{VACF}_{\text{solid}}(\omega)$ will be negative over a wide range of frequencies, which is unphysical. The results here satisfy this test, suggesting the soundness of this decomposition and the reasonableness of the choice of IF as a bridge between INM(ω) and VACF(ω).

Prior works have attempted to relate self-diffusion coefficients, D, of liquids to the fraction of imaginary modes over the total number of modes, $N_i + N_r$, similar to our IF_{alt} [12,20,21]. Some have proposed that D is linearly proportional to this fraction [12] while others have suggested subtler relations between D and the fraction of "delocalized" imaginary modes [21]. However, INM(ω) for our high-temperature liquid and gas systems challenges these ideas: (1) we see a dramatic slowing of how fast the density of states changes with temperature, as evident in Fig. 3(a), where temperature increases evenly by a factor of 10 but self-diffusion coefficients at these temperatures continue to increase with temperature as shown in the Appendix Sec. 3. (2) Nearly all imaginary modes in gas states at high temperatures are localized as confirmed by their inverse participation ratios [17].

More recently, Zaccone and Baggioli reported a linear power law at low frequencies in INM(ω) [16] and suggested that imaginary modes are important in describing heat capacity in liquids [37]. However, their work relies on empirical model fitting, leading to difficulties in understanding the nature of the heat carriers in liquids. Schirmacher *et al.* emphasized the importance of relative shapes of real and negative eigenvalue distributions of the dynamical matrices in understanding the nature of vibrational modes in liquids and how they become more symmetric with increase in temperature in liquids above glass transition temperatures [15]. Rather than characterizing specific shapes of certain instantaneous normal mode spectra, we focus on understanding the demographics of total number of atomic degrees of freedom in liquids: solidlike or gaslike. We have thus introduced a microscopically derived function describing "gasness" of a system designated as instability factors.

IV. CONCLUDING REMARKS

In summary, we have addressed thermodynamics of liquids in the context of both solid and gas phases. We propose to characterize the effective heat carriers in liquids via microscopically derived instability factors describing "gasness" in instantaneous normal mode spectra. In our approach we interpret instantaneous normal modes reflecting the local curvature of the potential energy landscape, rather than considering the instantaneous normal modes with real frequencies equivalent to harmonic oscillators in solids as is often done in the literature. We provide evidence in support of our proposal by good agreement between predicted specific heat values with those calculated from molecular dynamics. Our work provides insights into the long-standing problem of thermodynamics of liquids and suggests pathways to a unified framework in studying thermodynamics of solid, liquid, and gas phases.

In addition to conventional solid, liquid, and gas phases, we expect that our work could also be useful in studying thermodynamics and thermal properties of nonconventional materials including liquid crystals and solid ionic conductors. There have been many recent research interests in thermoelec-

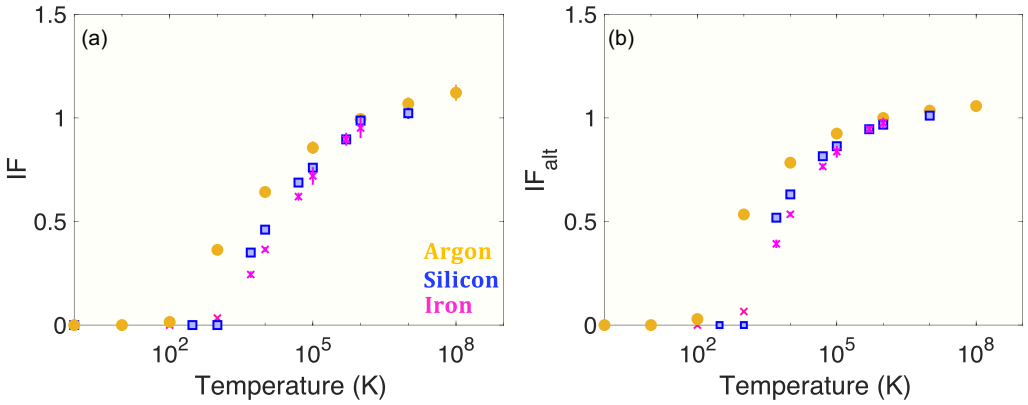

FIG. 8. Temperature-dependent instability factors for all ρ_0 systems. Yellow circles, blue squares, and pink crosses are for argon, silicon, and iron, respectively.

tric power generators in certain solid ionic conductors dubbed "phonon-liquid, electron crystal" where atoms at sublattice sites are fixed while others are diffusing [38–40]. This leads to desirable low heat capacity and nonelectronic thermal conductivity, but the origin of these is not yet clear. It is possible that our work helps identify the mechanism behind these complex phenomena.

ACKNOWLEDGMENTS

We are grateful for discussions with Alan McGaughey. This research was supported by the U.S. Department of Energy, Office of Science, Basic Energy Sciences, Materials Sciences and Engineering Division. This work used the Extreme Science and Engineering Discovery Environment (XSEDE) Expanse under Allocation No. TG-MAT200012. This research used resources of the National Energy Research Scientific Computing Center (NERSC), a U.S. Department of Energy Office of Science User Facility located at Lawrence Berkeley National Laboratory, operated under Contract No. DE-AC02-05CH11231 using NERSC Award No. BES-ERCAP0023621.

APPENDIX

1. Pair distribution functions for ρ_0 systems

To demonstrate that we are sampling different liquid and gas states, we examine pair distribution functions (PDFs), $g(r)$, of all ρ_0 systems shown in Fig. 7. As we increase the temperature, we observe progressive disappearance of well-defined peaks and valleys in the $g(r)$, highlighting a transition from liquid to dense gas states. The first distance point at which $g(r)$ becomes finite also decreases with increase in temperature as the distance at which potential energy $\sim k_B T$ becomes smaller, as expected. Thus, effective atomic diameters are getting smaller with increase in temperature, and the packing factor, the fraction of volume occupied by atoms, becomes smaller. Thus, the system makes a gradual transition from a liquidlike state to a gaslike state. At the same time, the repulsive part of the interatomic potential, $U(r)$, becomes increasingly important. The compressibility factor, $Z = \frac{pV}{Nk_B T}$, which is a measure of ideal gasness, is around 1.05 for the highest temperatures for all systems, confirming that our systems are indeed in gas states despite the high number density.

2. Size effects in normal modes and instability factors for ρ_0 systems

We have done lattice dynamics calculations on small systems consisting of ∼600 atoms and larger systems of ∼8000 atoms at select temperatures for which we did not observe qualitative differences in the spectral distributions between the small (600) and large (8000) systems. We expect slight size effects at low frequencies below a few THz; however, low frequency modes constitute a small portion of the overall mode population and should not generally affect our results. In addition, specific heat does not have strong size effects when normalized by number of atoms, so calculations on systems with ∼2000 atoms are sufficient here.

Temperature dependence of instability parameters are shown in Fig. 8. We observe a clear slowdown in increase in instability factors with temperature around IF = 1. Instability factors are slightly above 1 at high temperatures. We believe that this is due to relatively small system domain sizes. To ad-

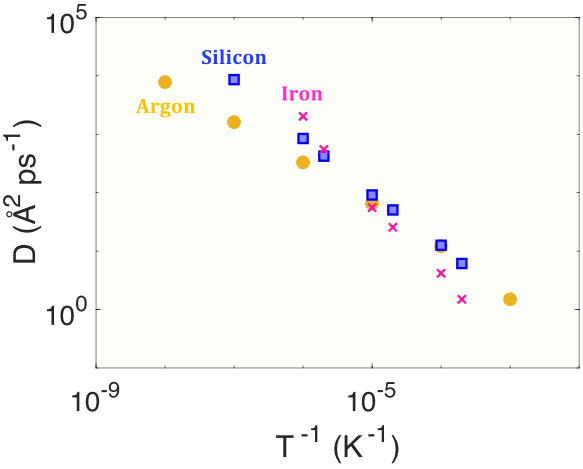

FIG. 9. Temperature-dependent self-diffusion coefficients, D, for all ρ_0 systems. Yellow circles, blue squares, and pink crosses are for argon, silicon, and iron, respectively. Monotonic increase in D with increase in temperature is observed.

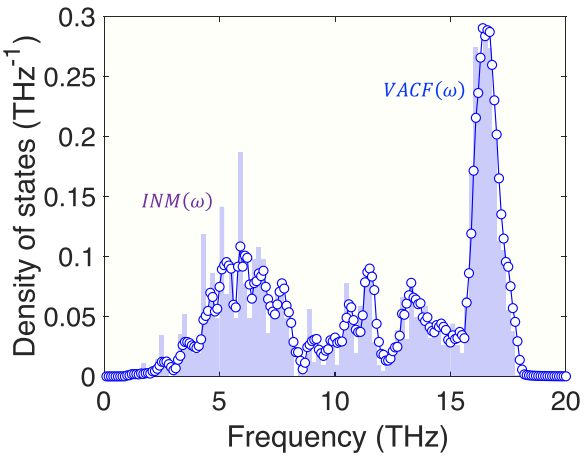

FIG. 10. Phonon density of states for crystalline silicon at 1 K. Nearly identical spectra between INM(ω) and VACF(ω) are seen, as expected.

equately test this issue, we would need to do lattice dynamics calculations on much bigger systems of $N = 10^4$ to $N = 10^6$ atoms; however, diagonalizing such large $3N$ by $3N$ matrices is challenging.

3. Diffusion coefficients and instability factors for NVT systems

Temperature-dependent self-diffusion coefficients, D, for all ρ_0 systems were calculated by

$$D = \lim_{t\to\infty} \frac{1}{6t} \langle [\boldsymbol{r}_i(t) - \boldsymbol{r}_i(0)]^2 \rangle \tag{A1}$$

where t is time and $\boldsymbol{r}_i(t)$ is the time-dependent position of atom i. As shown in Fig. 9, we observe a continuous increase in D for all systems with increase in temperature. Error bars are smaller than the symbol sizes.

4. INM(ω) and VACF(ω) equivalence for solids

Instantaneous normal mode and velocity autocorrelation spectra for solids are known to be equivalent under harmonic approximations and are both used to obtain phonon density of states of solids. An example of this equivalence is shown in Fig. 10 for crystalline silicon at 1 K with the Stillinger-Weber potential treating the entire domain as a unit cell and considering the Γ-point only. In this work, we make connections between these seemingly different spectra in liquids and gases via instability factors characterizing the nature of the atomic degrees of freedom.

[1] D. F. Williams, L. M. Toth, and K. T. Clarno, *Assessment of Candidate Molten Salt Coolants for the Advanced High Temperature Reactor (AHTR)* (U.S. Department of Energy, Washington, DC, 2006).

[2] G. Li, Sensible heat thermal storage energy and exergy performance evaluations, Renewable Sustainable Energy Rev. **53**, 897 (2016).

[3] A. Einstein, Die plancksche theorie der strahlung und die theorie der spezifischen Wärme, Ann. Phys. **327**, 180 (1907).

[4] P. Debye, Zur Theorie der spezifischen Wärmen, Ann. Phys. **344**, 789 (1912).

[5] M. T. Dove, *Introduction to Lattice Dynamics*, Cambridge Topics in Mineral Physics and Chemistry Vol. 4 (Cambridge University Press, Cambridge, 1993).

[6] A. Togo and I. Tanaka, First principles phonon calculations in materials science, Scr. Mater. **108**, 1 (2015).

[7] J. D. Gale, GULP: A computer program for the symmetry-adapted simulation of solids, J. Chem. Soc., Faraday Trans. **93**, 629 (1997).

[8] I. Pallikara, P. Kayastha, J. M. Skelton, and L. D. Whalley, The physical significance of imaginary phonon modes in crystals, Electron. Struct. **4**, 033002 (2022).

[9] T. Keyes, Instantaneous normal mode approach to liquid state dynamics, J. Phys. Chem. A **101**, 2921 (1997).

[10] R. M. Stratt, The instantaneous normal modes of liquids, Acc. Chem. Res. **28**, 201 (1995).

[11] M. Cho, G. R. Fleming, S. Saito, I. Ohmine, and R. M. Stratt, Instantaneous normal mode analysis of liquid water, J. Chem. Phys. **100**, 6672 (1994).

[12] G. Seeley, T. Keyes, and B. Madan, Isobaric diffusion constants in simple liquids and normal mode analysis, J. Chem. Phys. **95**, 3847 (1991).

[13] G. Seeley and T. Keyes, Normal-mode analysis of liquid-state dynamics, J. Chem. Phys. **91**, 5581 (1989).

[14] J. D. Gezelter, E. Rabani, and B. J. Berne, Can imaginary instantaneous normal mode frequencies predict barriers to self-diffusion? J. Chem. Phys. **107**, 4618 (1997).

[15] W. Schirmacher, T. Bryk, and G. Ruocco, Modeling the instantaneous normal mode spectra of liquids as that of unstable elastic media, Proc. Natl. Acad. Sci. USA **119**, e2119288119 (2022).

[16] A. Zaccone and M. Baggioli, Universal law for the vibrational density of states of liquids, Proc. Natl. Acad. Sci. USA **118**, e2022303118 (2021).

[17] J. Moon, L. Lindsay, and T. Egami, Atomic dynamics in fluids: Normal mode analysis revisited, Phys. Rev. E **108**, 014601 (2023).

[18] W. Zhang, J. F. Douglas, and F. W. Starr, What does the instantaneous normal mode spectrum tell us about dynamical heterogeneity in glass-forming fluids? J. Chem. Phys. **151**, 184904 (2019).

[19] A. Melzer, A. Schella, J. Schablinski, D. Block, and A. Piel, Instantaneous normal mode analysis of melting of finite dust clusters, Phys. Rev. Lett. **108**, 225001 (2012).

[20] E. L. Nave, A. Scala, F. W. Starr, F. Sciortino, and H. E. Stanley, Instantaneous normal mode analysis of supercooled water, Phys. Rev. Lett. **84**, 4605 (2000).

[21] V. I. Clapa, T. Kottos, and F. W. Starr, Localization transition of instantaneous normal modes and liquid diffusion, J. Chem. Phys. **136**, 144504 (2012).

[22] J. E. Jones, On the determination of molecular fields. II. From the equation of state of a gas, Proc. R. Soc. London A **106**, 463 (1924).

[23] J. E. Jones, On the determination of molecular fields. I. From the variation of the viscosity of a gas with temperature, Proc. R. Soc. London A **106**, 441 (1924).

[24] A. Rahman, M. J. Mandell, and J. P. McTague, Molecular dynamics study of an amorphous Lennard-Jones system at low temperature, J. Chem. Phys. **64**, 1564 (1976).

[25] S. Plimpton, Fast parallel algorithms for short-range molecular dynamics, J. Comput. Phys. **117**, 1 (1995).

[26] H. Stassen and Z. E. Gburski, Instantaneous normal mode analysis of binary liquid Ar-Kr mixtures, Chem. Phys. Lett. **217**, 325 (1994).

[27] P. G. Debenedetti and F. H. Stillinger, Supercooled liquids and the glass transition, Nature (London) **410**, 259 (2001).

[28] M. Goldstein, Viscous liquids and the glass transition: A potential energy barrier picture, J. Chem. Phys. **51**, 3728 (1969).

[29] E. P. Wigner, On the distribution of the roots of certain symmetric matrices, Ann. Math. **67**, 325 (1958).

[30] F. A. Lindemann, Über die Berechnung molekularer Eigenfrequenzen, Phys. Z. **11** (1910).

[31] F. H. Stillinger and T. A. Weber, Lindemann melting criterion and the Gaussian core model, Phys. Rev. B **22**, 3790 (1980).

[32] X. Fan, D. Pan, and M. Li, Rethinking Lindemann criterion: A molecular dynamics simulation of surface mediated melting, Acta Mater. **193**, 280 (2020).

[33] F. H. Stillinger and T. A. Weber, Computer simulation of local order in condensed phases of silicon, Phys. Rev. B **31**, 5262 (1985).

[34] D. Srolovitz, K. Maeda, V. Vitek, and T. Egami, Structural defects in amorphous solids statistical analysis of a computer model, Philos. Mag. A **44**, 847 (1981).

[35] V. A. Levashov, T. Egami, R. S. Aga, and J. R. Morris, Equipartition theorem and the dynamics of liquids, Phys. Rev. B **78**, 064205 (2008).

[36] D. Bolmatov, V. V. Brazhkin, and K. Trachenko, The phonon theory of liquid thermodynamics, Sci. Rep. **2**, 421 (2012).

[37] M. Baggioli and A. Zaccone, Explaining the specific heat of liquids based on instantaneous normal modes, Phys. Rev. E **104**, 014103 (2021).

[38] H. Liu, X. Shi, F. Xu, L. Zhang, W. Zhang, L. Chen, Q. Li, C. Uher, T. Day, and G. J. Snyder, Copper ion liquid-like thermoelectrics, Nat. Mater. **11**, 422 (2012).

[39] D. J. Voneshen, H. C. Walker, K. Refson, and J. P. Goff, Hopping time scales and the phonon-liquid electron-crystal picture in thermoelectric copper selenide, Phys. Rev. Lett. **118**, 145901 (2017).

[40] J. L. Niedziela, D. Bansal, A. F. May, J. Ding, T. Lanigan-Atkins, G. Ehlers, D. L. Abernathy, A. Said, and O. Delaire, Selective breakdown of phonon quasiparticles across superionic transition in $CuCrSe_2$, Nat. Phys. **15**, 73 (2019).